Nonlinear dynamics of a flexible rotor on tilting pad journal bearings experiencing rub–impact

Ebrahim Tofighi-Niaki, Pouya Asgharifard-Sharabiani & Hamid Ahmadian

Nonlinear Dynamics
An International Journal of Nonlinear Dynamics and Chaos in Engineering Systems

ISSN 0924-090X
Volume 94
Number 4

Nonlinear Dyn (2018) 94:2937-2956
DOI 10.1007/s11071-018-4535-0

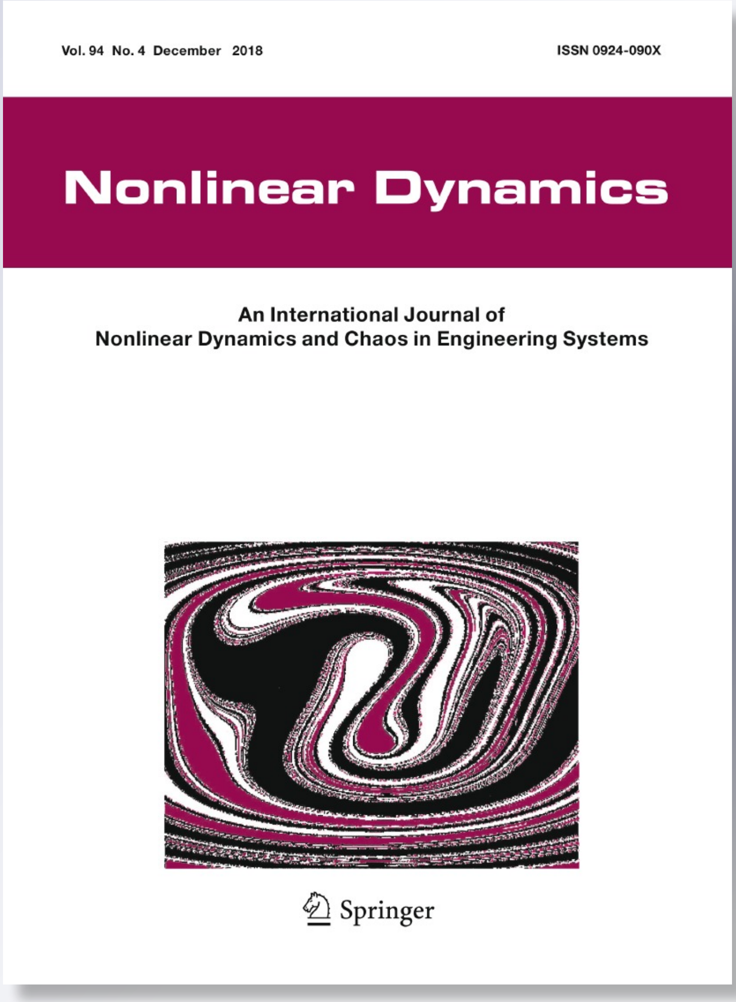

Springer

Your article is protected by copyright and all rights are held exclusively by Springer Nature B.V.. This e-offprint is for personal use only and shall not be self-archived in electronic repositories. If you wish to self-archive your article, please use the accepted manuscript version for posting on your own website. You may further deposit the accepted manuscript version in any repository, provided it is only made publicly available 12 months after official publication or later and provided acknowledgement is given to the original source of publication and a link is inserted to the published article on Springer's website. The link must be accompanied by the following text: "The final publication is available at link.springer.com".

Springer

Author's personal copy

Nonlinear Dyn (2018) 94:2937–2956
https://doi.org/10.1007/s11071-018-4535-0

ORIGINAL PAPER

Nonlinear dynamics of a flexible rotor on tilting pad journal bearings experiencing rub–impact

Ebrahim Tofighi-Niaki ·
Pouya Asgharifard-Sharabiani ·
Hamid Ahmadian

Received: 13 August 2017 / Accepted: 23 August 2018 / Published online: 15 September 2018
© Springer Nature B.V. 2018

Abstract Rub–impact phenomenon occurring in hydrodynamic journal bearings is one of the main malfunctions in rotating machines and causes undesirable dynamic behavior. In order to investigate such a phenomenon, nonlinear dynamics due to rub–impact within tilting pad journal bearings supporting a flexible rotor is studied. In simulating rub–impact between the journal and the associated pads, this paper employs mixed lubrication theory along with elasto-plastic asperity contact model between pads and journal. Periodic, quasiperiodic and chaotic vibrational behaviors of system are studied by varying the unbalanced load magnitude and the rotational speed of the rotor as control parameters. Phase plane orbits, waterfall frequency response spectra and bifurcation diagrams are used to show various dynamic responses of rotor when the control parameters are changed. The Poincaré maps are used to determine the onset of irregular motions. Presented results provide better understanding of strongly nonlinear vibrations occurring due to rub–impact in TPJBs supporting industrial rotating machines.

Keywords Asperity contact · Nonlinear dynamics · Oil film force · Rub–impact · Tilting pad journal bearings

List of symbols

$\bar{C}_{\mathrm{P}}$	Oil specific heat capacity
D_{s}	Shaft diameter
$D_{\mathrm{b}} = 2R_{\mathrm{b}},\ D_{\mathrm{j}} = 2R_{\mathrm{j}},\ D_{\mathrm{p}} = 2R_{\mathrm{p}}$	Diameters of bearing, journal and pads
$d^{*}_{\mathrm{e},k}$	Separation between the *k*th pad and journal
E'	Equivalent young modulus
E_{s}	Young modulus of shaft
$e = \sqrt{X_{\mathrm{j}}^{2} + Y_{\mathrm{j}}^{2}}$	Journal eccentricity
$\vec{e}_1$	Unit vector in the direction of journal velocity
F	Friction coefficient between journal and pads
f_{p}	Fractional rotational position of pivot
f^{*}	Normalized frequency
$\{F_{\mathrm{g.}}\},\ \{F_{\mathrm{nl.}}\},\ \{F_{\mathrm{unb.}}\}$	Force vectors due to gravity, nonlinearities and mass unbalance
$F_x,\ F_y$	Components of oil film forces in horizontal and vertical directions
$[G],\ [G]^{*}$	Physical and modal gyroscopic matrices

E. Tofighi-Niaki · P. Asgharifard-Sharabiani ·
H. Ahmadian (✉)
Center of Excellence in Experimental Solid Mechanics and Dynamics, School of Mechanical Engineering, Iran University of Science and Technology, Narmak, Tehran 16848, Iran
e-mail: ahmadian@iust.ac.ir

Author's personal copy

H_{a}	Hardness of the softer material
$H_{\mathrm{j}},\ H_{\mathrm{p1}}$	Heat convection coefficients of oil film over surfaces of journal and pads
$H_k = h_k/\sigma$	Non-dimensional oil film thickness on the *k*th pad
$h_k,\ \bar{h}_{\mathrm{T},k}$	Nominal and average oil film thickness on the *k*th pad
J	Moment of inertia of each tilting pad
$[K],\ [K]^*$	Physical and modal stiffness matrices
$L_{\mathrm{b}},\ L_{\mathrm{s}}$	Lengths of bearing and shaft
$[M],\ [M]^*$	Physical and modal mass matrices
M_k	Moment applied to the *k*th pad
$m_{\mathrm{d}},\ m_{\mathrm{j}}$	Masses of disk and journal
M	Preload
N_{pads}	Number of pads
$P_k,\ \bar{P}_k$	Local and mean hydrodynamic pressure distributions on the *k*th pad
$P_{\mathrm{a},k}$	Asperity contact pressure on the *k*th pad
$P_{\mathrm{e},k},\ \mathrm{P}_{\mathrm{p},k}$	Asperity contact pressures due to elastic and plastic deformations on the *k*th pad
$\{q(t)\}$	Vector of generalized coordinates
T_{J}	Journal surface temperature
$T^k,\ T^k_{\mathrm{Sp}}$	Temperature distributions in oil film and on the inner surface of *k*th pad
$t_{\mathrm{d}}, t_{\mathrm{P}}$	Thicknesses of disk and pads
$\{U(t)\}$	Time-dependent displacement vector
$V_1 = R_{\mathrm{j}}\omega$	Velocity of journal
$V_{2,k}$	Velocity of the *k*th pad projected on journal velocity direction
$w^*_{\mathrm{p}} = (\beta'/\sigma^*)(2H_{\mathrm{a}}/E')^2$	Plasticity index
$x = R_{\mathrm{j}}\theta, y, z$	Horizontal, vertical and axial coordinates
$X_{\mathrm{j}},\ Y_{\mathrm{j}},\ X_{\mathrm{d}},\ Y_{\mathrm{d}}$	Horizontal and vertical displacements of the journal and the disk
B	Thermo viscosity index
β'	Mean radius of asperities
δ_k	Tilt angle of the *k*th pad
η	Asperity density
θ	Bearing circumferential coordinate
$\theta^k_{\mathrm{p}},\ \theta^k_{\mathrm{l}},\ \theta^k_{\mathrm{t}}$	Pivoting, leading and trailing angles of the *k*th pad
$\mu,\ \mu_0$	Oil viscosities at temperatures T and T_0
$\sigma_1,\ \sigma_2$	Asperity height standard deviations of pads and journal
$\sigma = (\sigma_1^2 + \sigma_2^2)^{0.5}$	Root mean square (rms) of roughness standard deviations of surfaces of pads and journal
σ^*	Asperity summit height standard deviation
$\tau_{\mathrm{a},k'},\ \bar{\tau}_k$	Tangential asperity contact stress and mean hydrodynamic shear stress on the *k*th pad
ν	Poisson ratio
$[\Phi]$	Modal matrix
$\phi(s)$	Probability density function
ϕ_{s}	Couette shear flow factor
$\phi_\theta,\ \phi_z$	Pressure flow factors in circumferential and axial directions
$\phi_{\mathrm{fs}},\ \phi_{\mathrm{fp}}$	Shear stress factors
$\rho,\ \rho_{\mathrm{s}}$	Densities of oil and shaft
ω	Rotational speed of the rotor

1 Introduction

High-speed rotating machines often experience rub–impact malfunction between the rotor and the stator. This malfunction may be originated from deficiencies such as excessive unbalance, rotor permanent bow, misalignment and self-excited instability due to lubricat-

Author's personal copy

ing fluid. The dynamics of the machine during the rub–impact is strongly nonlinear leading to complex vibrations. Serious failures caused by this fault can be prevented by conclusions drawn from the rub–impact studies in rotor dynamic analysis.

There are abundant studies on nonlinear dynamics wherein strong nonlinearities due to hydrodynamic lubrication and rub–impact phenomenon are coupled together in the rotor–bearing system. In these studies, strong nonlinearities resulting from hydrodynamic lubrication occur inside journal bearings that support the rotor. The nature of this phenomenon is different from rub–impact between a disk located at the rotor midpoint and the stator. Analysis methods such as phase plane portrait, power spectrum, Poincaré map, bifurcation diagram and Lyapunov exponent are used to investigate the vibration behavior of the journal center and bearing center in the horizontal and vertical directions under various operating conditions. Chang-Jian and Chen [1–3] demonstrated the periodic, subharmonic, quasiperiodic and chaotic responses in a flexible rub–impact rotor supported by oil film short and long journal bearings with nonlinear suspension wherein the lubricating fluids were operating in laminar and turbulent regimes. They performed nonlinear dynamic analysis of rub–impact flexible rotor–bearing systems supported by two couple stress fluid film journal bearings with and without considering quadratic damping in different studies [4,5]. Floquet theory is employed by Wang et al. [6] to perform stability analysis of a rub–impact rotor supported by oil film bearings. The stability analysis revealed the existence of stable periodic motions in a large range of rotational speed and period-doubling bifurcations in some other speed ranges. Xiang et al. [7] conducted nonlinear dynamic analysis of a rotor–bearing system considering time-varying crack stiffness, rub–impact force along with employing the short bearing theory to describe the nonlinear oil film forces. They indicated that crack depth and stator stiffness made the system instable with varied rotational speed. Cao et al. [8] investigated rub–impact between rotor and stator incorporating fractionally damped rotor system. The damping model using fractional derivative has many practical applications in the mechanical engineering because it can be employed to describe the complicated frequency dependency of damping materials. They found that fractional-order damping rotor with rubbing faults can produce various types of complex dynamic behaviors including period-doubling bifurcation, sudden transition and quasiperiodic from periodic motion to chaos. Abu Arqub [9] introduced the reproducing kernel Hilbert space method for treating classes of time-fractional partial differential equations subject to Neumann boundary conditions with parameters derivative arising in a wide range of applications. Arqub et al. [10] proposed a new analytical technique based on the generalized Taylor series formula and residual error function, for constructing and predicting solitary pattern solutions of time-fractional dispersive partial differential equations. El-Ajou et al. [11] presented explicit and approximate solutions of the nonlinear fractional KdV–Burgers equation with time–space-fractional derivatives based on the generalized Taylor series formula. In aforementioned studies, the rub–impact force obeys the elastic Hertz contact relation along with velocity-dependent Coulomb friction law.

In present models, surface roughness effects that exist in practical applications are not considered in evaluating the rub–impact forces. Incorporating surface roughness effects into analysis of rub–impact phenomena may provide useful insight into contact mechanism between rotary parts and stationary parts of rotating machines. Although analysis of nonlinear dynamics induced by rub–impact phenomena between the rotating part and the stationary part is performed in the literature, there is lack of studies wherein contact between the rotating journal and the tilting pad in the journal bearing. Simulating contact between lubricated surfaces is affected by the surface roughness. Thus, roughness effects of the journal and the bearing are considered in the present study in hydrodynamic analysis of the lubricant flow and simulating rub–impact occurring within the oil film bearing.

When a journal comes into contact with a bearing surface, the dynamics of the rotor–bearing system is influenced by surface roughness effect on the lubricant flow and the asperity contact pressure induced between contacting surfaces. Three types of lubrication regime between two rough surfaces are described in the literature [12]. When two surfaces of lubrication are far enough and contact between asperities does not occur, surfaces are in hydrodynamic lubrication regime. In this situation, ratio of average oil film thickness, h, to asperities standard deviation, σ, is $H = h/\sigma \geq 3$. When the values of H become less than 3, contact between asperities height begins and the

Author's personal copy

regime of lubrication is changed to mixed lubrication. Once the ratio of H becomes below 0.5, mixed lubrication formulation is no longer reliable and the lubricating flow begins to operate in boundary lubrication regime. Patir and Cheng [13,14] proposed an average flow model to solve for pressure distributions in lubricated sliding surfaces with roughness which is appropriate for simulating mixed lubrication regime. On the other hand, Greenwood and Williamson [15] presented a model for the asperity contact mechanism of non-lubricated rough surfaces. Johnson et al. [16] combined the Greenwood and Williamson theory of contact of random rough surface with established elasto-hydrodynamic theory to provide a theoretical approach to highly loaded lubricated contacts in which the load is shared between hydrodynamic pressure and asperity contact. Yamaguchi and Matsuoka [17] investigated the contact between two rough surfaces in a journal bearing operating in mixed and hydrodynamic lubrication regimes. Ai et al. [18] studied a dynamical loaded journal behavior in mixed lubrication condition with finite element method. Kazama and Naritia [19] investigated steady-state characteristics of worn plain journal bearings using the approaches proposed in [14,16]. Sander et al. [20] simulated friction induced between a bearing and its associated journal and validated the results with experimental measurements. Leighton et al. [21] presented a method based on the approach introduced in [15] to model asperity interactions of real rough surfaces using the measured surface topography. The proposed model made realistic predictions for load carrying and frictional performance in real applications through comparing the numerical results with the experiment. Varney and Green [22] used the elasto-plastic rough surface contact model which relies on measurable surface parameters to calculate the contact force in dynamic analysis of rotor–stator rub.

In this paper, nonlinear dynamics of a flexible rotor–bearing system equipped with two tilting pad journal bearings (TPJBs) experiencing rub–impact is studied. The journal and the pads are considered to have rough surfaces. Also, large amplitudes of vibrations at TPJBs result in an H of less than 3. Therefore, mixed lubrication model is required to simulate the lubricating flow and asperity contact model governs the impact between the journal and the pads. Owing to the widespread use of TPJBs in industrial rotating machines for their excellent stability, high radial load capacity and high-speed operating condition, this type of journal bearing is employed to support the underlying flexible rotor.

The rest of this manuscript is organized as follows. In Sect. 2, mathematical model used to simulate the hydrodynamic lubrication and rub–impact between the journal and the pads inside a typical TPJB are illustrated. Numerical results obtained from nonlinear dynamics analysis of rub–impact occurring inside TPJBs supporting a flexible rotor are presented in Sect. 3. Finally, a brief conclusion is made in Sect. 4.

2 Mathematical modeling

2.1 Model description

A flexible rotor supported by two identical TPJBs is shown in Fig. 1. The rotor under study consists of a continuous flexible shaft and a rigid disk located at the rotor midpoint. As the journal and the pads are assumed to have rough surfaces, the mean lubricant flow model proposed in [13,14] is employed to evaluate the nonlinear oil film forces. Rub–impact forces

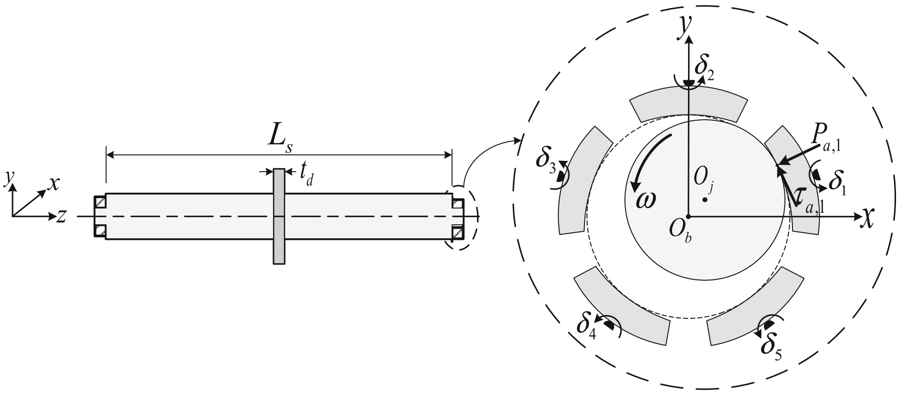

Fig. 1 Model of a flexible rotor supported by two TPJBs

Author's personal copy

induced between the journal and the pads are calculated using the asperity contact mechanism introduced in [15]. In the present work, the lubricant flow operates in laminar regime and is assumed to be incompressible. In general, non-rotating and rotating damping forces in rotor dynamics cause the symmetric damping matrix and the skew-symmetric circulatory matrix to be considered in system governing equations. These matrix terms may be included in modeling of the present rotating system due to the hysteretic damping of the shaft. Since the structural damping forces due to the shaft hysteretic damping are in lower order of magnitude compared to the viscous damping forces induced by the TPJBs, the structural damping effect of the shaft is ignored in the present study. The governing equations of the undamped flexible rotor resting on two TPJBs are:

$$[M]\{\ddot{U}(t)\} + \omega[G]\{\dot{U}(t)\} + [K]\{U(t)\} = \{F_{\text{unb}}\} + \{F_{\text{g}}\} + \{F_{\text{nl}}\}, \tag{1}$$

$$J\ddot{\delta}_l = M_l, l = 1, \ldots, N_{\text{pads}}, \tag{2}$$

$$J\ddot{\delta}_l = M_r, r = 1, \ldots, N_{\text{pads}}, \tag{3}$$

where $[M]$, $[G]$ and $[K]$ represent the mass, gyroscopic and stiffness matrices of the flexible rotor; J is the moment of inertia of each tilting pad; $\{F_{\text{unb}}\}$, $\{F_{\text{g}}\}$ are the vectors of the unbalanced load, gravitational force; $\{F_{\text{nl}}\}$ is the nonlinear force vector due to hydrodynamic force and elasto-plastic contact between the journal and the pads; M_l and M_r are the nonlinear moments applied to the lth pad and rth pad of the left and right TPJBs; $\{U(t)\}$ is the rotor displacement vector; δ_l and δ_r are the tilt angles related to the lth pad and rth pad of the left and right TPJBs; ω is the rotor rotational speed; t is the time variable; the over-dot $(\cdot)$ represents time derivative. The model expressed in Eqs. (1)–(3) constitutes a coupled nonlinear system of ordinary differential equations, wherein the nonlinear force vector, $\{F_{\text{nl.}}\}$, includes nonlinear forces and moments acting on the journal and the pads. These nonlinear forces and moments are caused by hydrodynamic lubrication and rub–impact between the journal and the TPJB. The transient response of the system defined in Eqs. (1)–(3) is expanded in the form:

$$\{U(t)\} = [\Phi]\{q(t)\}, \tag{4}$$

where $\{q(t)\}$ represents the vector of generalized coordinates. Columns of the modal matrix $[\Phi]$ in Eq. (4) are eigenvectors obtained from eigenanalysis of the flexible rotor supported by TPJBs in non-rotating condition. Inserting the modal expansion of Eq. (4) into the system governing equations [Eqs. (1)–(3] and pre-multiplying the governing equations of motion by $[\Phi]^T$, they transformed to modal domain as:

$$[M]^*\{\ddot{q}\} + \omega[G]^*\{\dot{q}\} + [K]^*\{q\} = [\Phi]^T(\{F_{\text{unb}}\} + \{F_{\text{g}}\} + \{F_{\text{nl}}\}), \tag{5}$$

$$J\ddot{\delta}_l = M_l, l = 1, \ldots, N_{\text{pads}}, \tag{6}$$

$$J\ddot{\delta}_r = M_r, r = 1, \ldots, N_{\text{pads}}, \tag{7}$$

where

$$[M]^* = [\Phi]^T[M][\Phi], \tag{8}$$

$$[G]^* = [\Phi]^T[G][\Phi], \tag{9}$$

$$[K]^* = [\Phi]^T[K][\Phi]. \tag{10}$$

2.2 Mixed lubrication regime

Oil film thickness inside the kth pad of the TPJB is expressed by:

$$h_k = (R_{\text{p}} - R_{\text{j}}) - X_{\text{j}}\cos\theta - Y_{\text{j}}\sin\theta - (R_{\text{p}} - R_{\text{b}})\cos(\theta - \theta_{\text{p}}^k) - \delta_k(R_{\text{p}} + t_{\text{p}})\sin(\theta - \theta_{\text{p}}^k), \tag{11}$$

where X_{j} and Y_{j} represent the horizontal and vertical position of the journal center; R_{p}, R_{j} and R_{b} are radii of the pad, the journal and the bearing, respectively; θ_{p}^k is the pivoting angle of the kth pad; t_{p} is the pad thickness; θ represents the bearing circumferential coordinate. Using the expression for oil film thickness in Eq. (11), transient mean hydrodynamic pressure within the TPJB considering surface roughness is obtained by finding the solution to unsteady 2-D average Reynolds equation as [13,14]:

$$\begin{aligned} &\frac{1}{R_{\text{j}}^2}\frac{\partial}{\partial\theta}\left(\phi_\theta\frac{h_k^3}{12\mu}\frac{\partial\bar{P}_k}{\partial\theta}\right) + \frac{\partial}{\partial z}\left(\phi_z\frac{h_k^3}{12\mu}\frac{\partial\bar{P}_k}{\partial z}\right) \\ &\quad = \frac{V_1 + V_{2,k}}{2}\frac{\partial(\rho\bar{h}_{\text{T},k})}{\partial z} \\ &\qquad + \frac{V_1 - V_{2,k}}{2}\sigma\frac{1}{R_{\text{j}}}\frac{\partial\phi_{\text{s}}}{\partial\theta} + \frac{\partial(\rho\bar{h}_{\text{T},k})}{\partial t}; \\ &\qquad \theta_l^k \le \theta \le \theta_t^k, 0 \le z \le L_{\text{b}}; \\ &\qquad k = 1, \ldots, N_{\text{pads}}, \end{aligned} \tag{12}$$

where $\bar{P}_k$ is the mean hydrodynamic pressure distributions on the kth pad; ϕ_θ and ϕ_z represent pressure

Author's personal copy

flow factors in circumferential and axial directions; ϕ_s is the shear flow factor which are given in [13,14]; μ is the oil film viscosity; σ is the rms of roughness standard deviations of surfaces of the pads and the journal; V_1 is the journal surface velocity; $V_{2,k}$ represents the velocity of the surface of the kth pad in direction of the journal surface velocity; ρ is oil film density; θ_l^k and θ_t^k are leading and trailing angles of the kth pad; z is the axial coordinate; L_b is the bearing length. Average oil film thickness on the kth pad in Eq. (12) is determined as:

$$\bar{h}_{\mathrm{T},k} = \begin{cases} h_k; & H_k \geq 3 \\ \frac{3\sigma}{256}(35 + w\,(128 + w\,(140 + w^2 \\ \quad (-70 + w^2(28 - 5w^2))))); & H_k \leq 3, \end{cases} \tag{13}$$

where $w = H_k/3$. The lubricant in the present model is considered as temperature dependent. In order to consider these variations, thermo-hydrodynamic (THD) analysis is performed by satisfying the steady-state Reynolds equation, one-dimensional heat equation and the static equilibrium equations following the procedure illustrated in [23]. THD analysis at each rotational speed results in circumferential temperature distribution inside the oil film and the static equilibrium position of the TPJB. Thermal effects in evaluating transient mean hydrodynamic pressure are applied by putting the obtained circumferential variations of the oil film viscosity into the average Reynolds equation [Eq. (12)].

Using the mean lubricant flow mode presented in [13,14], mean hydrodynamic shear stress acting on the mating surfaces of the journal and the kth pad is determined by:

$$\bar{\tau}_k = \mu \frac{V_1 - V_{2,k}}{h_k}(\phi_\mathrm{f} \pm \phi_\mathrm{fs}) \pm \phi_\mathrm{fp} \frac{h_k}{2}\frac{\partial \bar{P}_k}{\partial x}; \quad k = 1, \ldots, N_\mathrm{pads}, \tag{14}$$

where ϕ_f, ϕ_fs and ϕ_fp represent the shear flow factors which are given in [13,14]. The positive and negative signs in Eq. (14) are referred to mean shear stress on the surfaces of the kth pad and the journal, respectively. Finite element method is employed to solve the average Reynolds equation for the pressure distributions inside the TPJB.

2.3 Contact modeling between journal and TPJB

In this study, asperity contact model is used to simulate contact between the journal and the pads in the TPJB. In general, surfaces of the journal and the pads are considered as nominally flat metal surfaces with the specified roughness. These rough surfaces are assumed to be covered with asperities which have spherically shaped summits. Under large amplitudes of vibrations, rough surfaces become very close to each other. Subsequently, contact between asperities begins to occur, and the asperities have undergone elastic and plastic deformations. Greenwood and Williamson [15] used Hertz contact theory to develop a model for calculation of contact pressure between two rough surfaces. They assumed the contact of two rough surfaces can be regarded as a contact between an equivalent rough surface and a smooth surface. Therefore, contact pressures resulting from elastic and plastic deformations of asperities in the surfaces of the journal and the pads induce rub–impact forces. Expressions for calculating the elasto-plastic contact pressure between rough surfaces of the journal and the kth pad are as [16,17]:

$$P_{\mathrm{a},k} = P_{\mathrm{e},k} + P_{\mathrm{p},k}; \quad k = 1, \ldots, N_\mathrm{pads}, \tag{15}$$

$$P_{\mathrm{e},k} = \frac{2}{3}E'\eta\beta'\sigma^* \left(\frac{\sigma^*}{\beta'}\right)^{1/2} \left[F_{3/2}(d^*_{\mathrm{e},k}) - F_{3/2}(d^*_{\mathrm{e},k} + w^*_\mathrm{p})\right], \tag{16}$$

$$P_{\mathrm{p},k} = \pi H_\mathrm{a}\eta\beta'\sigma^* F_1(d^*_{\mathrm{e},k} + w^*_\mathrm{p}), \tag{17}$$

where $P_{\mathrm{a},k}$ is the total contact pressure on the kth pad; $P_{\mathrm{e},k}$ and $P_{\mathrm{a},k}$ represent asperity contact pressures on the kth pad due to elastic and plastic deformations; β' is the equivalent asperity summit height; η represents the asperity density in unit area; σ^* is the standard deviation of the asperity summit height; H_a is the Brinell hardness of the softer material; w^*_p is represent the plasticity index. A detailed description of the relations for elasto-plastic contact pressure between rough surfaces may be found in Refs. [16,17]. Whitehouse and Archard [24] showed that the value of $\eta\beta'\sigma^*$ is constant and its value is equal to 0.05 for freshly grounded engineering surfaces. A comprehensive explanation of Hertz contact theory is given in [25]. Equivalent elastic modulus of two contacting surfaces is determined as:

$$\frac{1}{E'} = \frac{1}{2}\left(\frac{1 - \upsilon_1^2}{E_1} + \frac{1 - \upsilon_2^2}{E_2}\right). \tag{18}$$

Subscripts 1 and 2 in Eq. (18) refer to the journal and the pads, respectively. Non-dimensional separation between two rough surfaces is evaluated by:

Author's personal copy

Table 1 Rotor–bearing system properties

Rotor		Bearing	
Parameter	Value	Parameter	Value
E_s (GPa)	200	f_p	0.5
ρ_s (kg m^{-3})	8000	D_b (mm)	125.196
ν	0.3	L_b (mm)	50
D_j (mm)	125	M	0.3988
D_s (mm)	160	θ_p (°)	18, 90, 162, 234, 306
L_s (m)	1.84	Δ_p (°)	52
t_d (m)	0.08	J_p (kg m^2)	0.0024
σ_2 (µm)	0.4	σ_1 (µm)	0.4
m_d (kg)	176.4	m_j (kg)	687.982

Table 2 Thermal and surface texture properties

Thermal properties		Surface texture properties	
Parameter	Value	Parameter	Value
$\bar{C}_\mathrm{P}$ (J Kg^{-1} K^{-1})	2000	$\eta\beta'\sigma^*$	0.05
ρ (kg m^{-3})	860	E' (GPa)	222.31
β (C^{-1})	0.0319	F	0.1
μ at 40 °C (Pa s)	0.0396	H_a (MPa)	493

$$d^*_{\mathrm{e},k} = \begin{cases} H_k; & H_k \geq 1.8 \\ 1.5H_k - 0.9; & H_k < 1.8. \end{cases} \tag{19}$$

The distribution of heights and peaks of the asperities on freshly grounded engineering surfaces is expected to obey Gaussian distribution. However, frequent contact between adjacent surfaces occurring in mixed lubrication regime may lead to change in the asperity distribution. Without loss of generality, it is assumed that in the present analysis that the surfaces have not worked for a long time in mixed lubrication regime. Thus, rough surfaces of the journal and the pads are considered to have Gaussian distribution with constant value of asperity heights during the operating condition. The function F_m in Eqs. (16) and (17) is described as:

$$F_\mathrm{m}(u) = \int_u^\infty (s-u)^m \phi(s)\mathrm{d}s;$$
$$\phi(s) = \frac{1}{\sqrt{2\pi}}\exp\left(-\frac{s^2}{2}\right). \tag{20}$$

The integral of the Gaussian distribution in Eq. (20) can be computed as described in [15], and the corresponding values are tabulated in Ref. [26]. Asperity contact pressures induced between two metallic rough surfaces are determined applying Eqs. (15)–(20). Using the contact pressure expression in Eq. (15), tangential asperity contact stress between rough surfaces of the journal and the kth pad is obtained by [18]:

$$\tau_{\mathrm{a},k} = f P_{\mathrm{a},k}, \tag{21}$$

where f is the friction coefficient. Finally, mean hydrodynamic pressure and tangential asperity contact stress resulting from Eqs. (12) and (21), respectively, are integrated over the area of the pads to give oil film and rub–impact forces and moments as:

$$F_x = -\sum_{k=1}^{N_\mathrm{pads}} \int_{-\frac{L}{2}}^{\frac{L}{2}} \int_{\theta_l}^{\theta_t} ((P_{\mathrm{a},k} + \bar{P}_k)\cos\theta$$
$$- \operatorname{sign}((\vec{V}_1 - (\vec{V}_{2,k}\cdot\vec{e}_1)\vec{e}_1)\cdot\vec{e}_1)\,(\tau_{\mathrm{a},k} + \bar{\tau}_k)\sin\theta)$$
$$R_\mathrm{j}\mathrm{d}\theta\mathrm{d}z, \tag{22}$$

$$F_y = -\sum_{k=1}^{N_\mathrm{pads}} \int_{-\frac{L}{2}}^{\frac{L}{2}} \int_{\theta_l}^{\theta_t} ((P_{\mathrm{a},k} + \bar{P}_k)\sin\theta$$
$$+ \operatorname{sign}((\vec{V}_1 - (\vec{V}_{2,k}\cdot\vec{e}_1)\vec{e}_1)\cdot\vec{e}_1)\,(\tau_{\mathrm{a},k} + \bar{\tau}_k)\cos\theta)$$
$$R_\mathrm{j}\mathrm{d}\theta\mathrm{d}z, \tag{23}$$

$$M_k = -\int_{-\frac{L}{2}}^{\frac{L}{2}} \int_{\theta_\mathrm{l}}^{\theta_\mathrm{t}} \Big[-(R_\mathrm{j} + t_\mathrm{p})(\theta - \theta_\mathrm{p}^k)(P_{\mathrm{a},k} + \bar{P}_k)$$
$$-\operatorname{sign}((\vec{V}_1 - (\vec{V}_{2,k}\cdot\vec{e}_1)\vec{e}_1)\cdot\vec{e}_1)t_\mathrm{p}\,(\tau_{\mathrm{a},k} + \bar{\tau}_k)\Big]$$
$$\cos(\theta - \theta_\mathrm{p})R_j\mathrm{d}\theta\mathrm{d}z;\ k = 1, \ldots, N_\mathrm{pads}, \tag{24}$$

where the vector $\vec{e}$ represents a unit vector in the direction of the journal absolute velocity at the point of contact between the journal and the kth pad. Derivation of expressions for the oil film and rub–impact forces and moments is illustrated in "Appendix." It is noted the right direction for the tangential stress in Eqs. (22)–(24) is shown to be in the opposite direction of relative velocity of the journal with respect to the pad.

3 Results and discussion

In the present study, nonlinear dynamics due to rub–impact within TPJBs supporting a flexible rotor is investigated numerically. The rotational speed of the shaft and the mass unbalance applied at the rotor disk are considered as control parameters. The numerical analysis is performed by using differential solver routine ode15s. The time step used for numerical integration in each run is assigned to be 1/1000 of the asso-

Author's personal copy

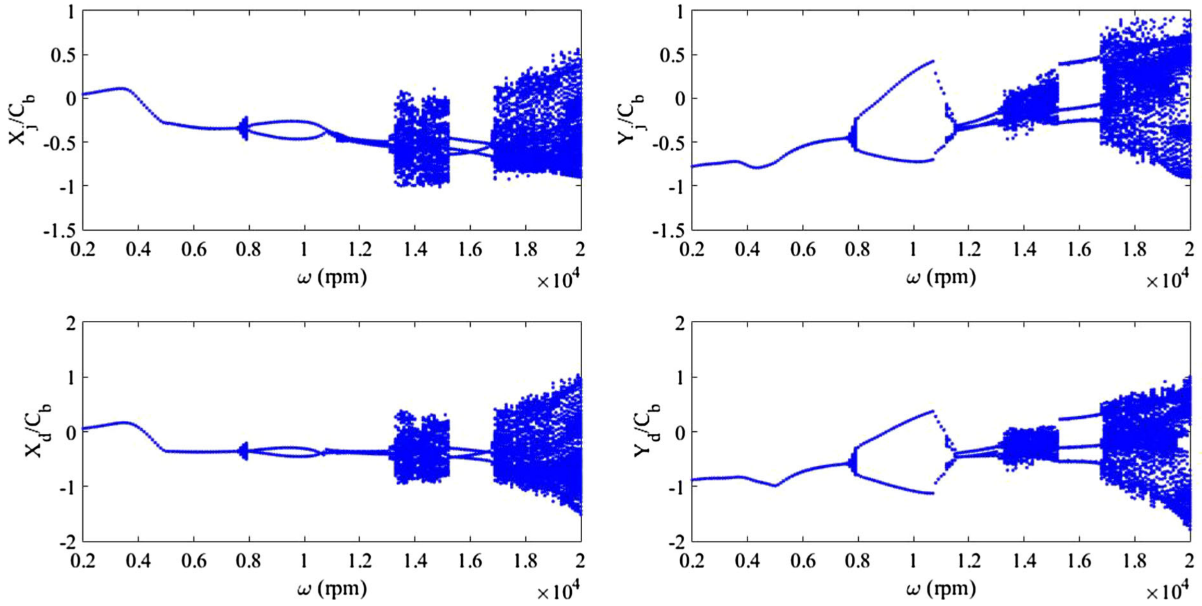

Fig. 2 Bifurcation diagrams of the journal center and the disk center in horizontal and vertical directions at me = 0.0346 kg m

Fig. 3 Mean impact force during the steady-state period versus the rotational speed at me = 0.0346 kg m

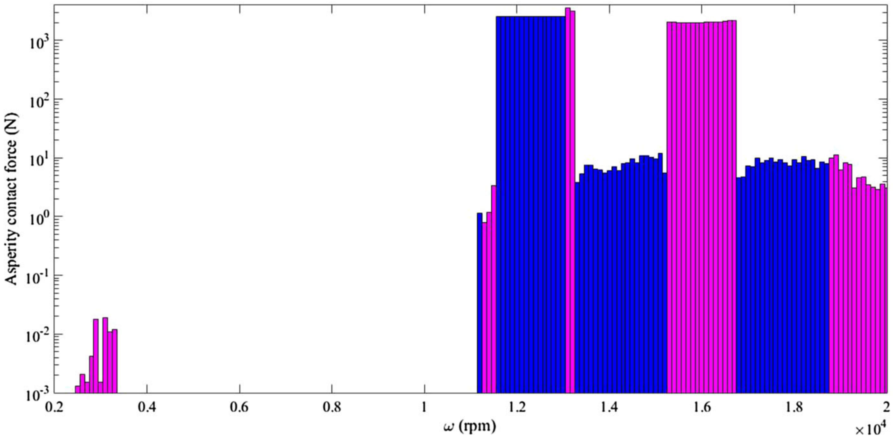

ciated prime period. Reaching the steady-state condition is guaranteed by neglecting the first few transient time response. The nonlinear dynamic response of the rotor–bearing system is illustrated by displacement and velocity orbits, waterfall frequency response spectra, Poincaré maps and bifurcation diagrams.

Parameter values of the rotor–bearing system, thermal and surface texture properties are given in Tables 1 and 2, respectively. As shown in Fig. 1, the flexible rotor is supported by two similar TPJBs.

3.1 Effect of rotational speed on the rotor response

Rotational speed of the rotor is one of the most effective factors on dynamics of rotating machines. Bifurcation diagrams for the present rotor–bearing system with rotational speed, varying in $\omega = [2000–20{,}000]$ rpm, as control parameter and mass unbalance me = 0.0346 kg m, are shown in Fig. 2. Because the TPJBs supporting the flexible rotor at its both ends are similar and the unbalanced load is applied to the rotor at the midpoint, the implemented eigenvectors in the modal matrix are confined to the corresponding rigid mode shape and the first bending mode shape.

Author's personal copy

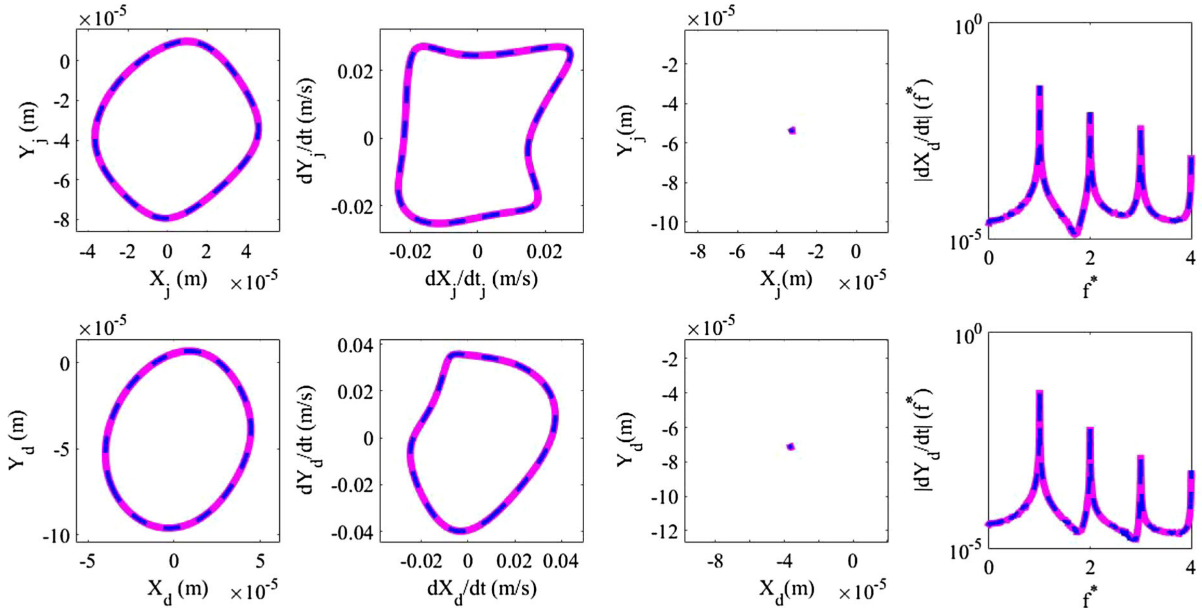

Fig. 4 Phase plane orbits, Poincaré maps and frequency spectra at $\omega = 6000$ rpm (smooth surface assumption: magenta solid line; rough surface assumption: blue dash line). (Color figure online)

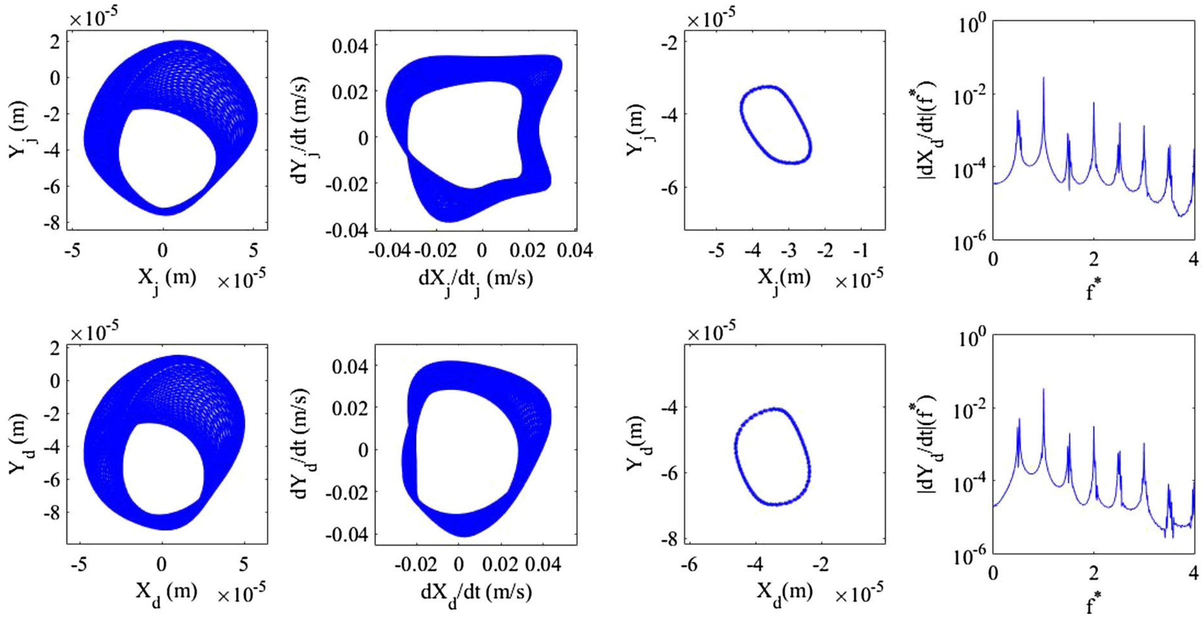

Fig. 5 Phase plane orbits, Poincaré maps and frequency spectra at $\omega = 7800$ rpm

The changes in dynamics of journal center and disk center displacements in horizontal and vertical directions by varying the rotational speed of the shaft and through sampling periodically, with the same period as rotational speed, from the rotor response time series are shown in Fig. 2. The mean impact force induced by asperity contact at a constant rotational speed is evaluated during the corresponding steady-state period. Variations of the mean impact force versus the rotational speed are displayed in Fig. 3. Successive bifurcations

Author's personal copy

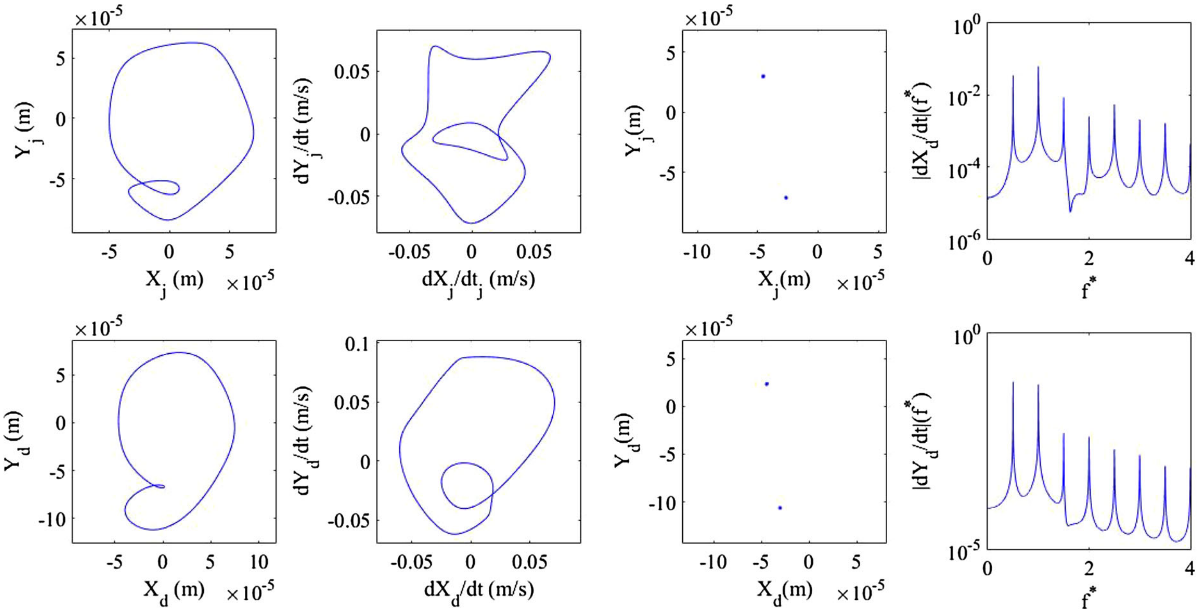

Fig. 6 Phase plane orbits, Poincaré maps and frequency spectra at $\omega = 10{,}000$ rpm

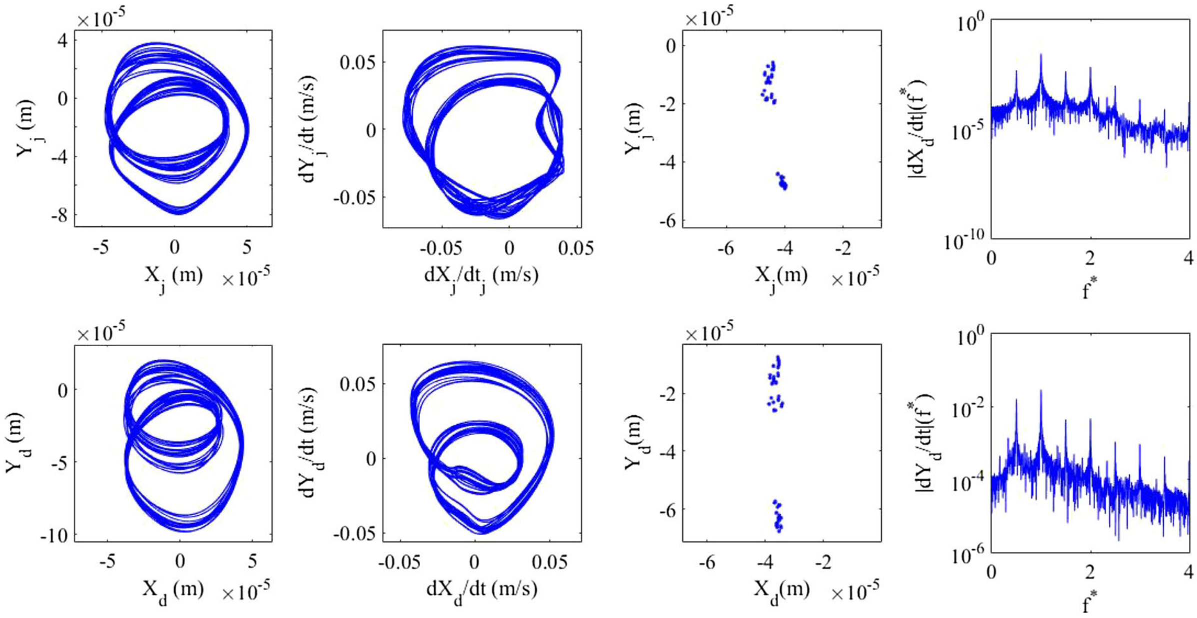

Fig. 7 Phase plane orbits, Poincaré maps and frequency spectra at $\omega = 11{,}200$ rpm

of the system dynamic behavior depicted in Fig. 2 are indicated by two different colors of blue and magenta in Fig. 3.

For period-n (Pn) motion, the return points on the Poincaré map are n isolated points. Figure 2 shows that the dynamics of the system is harmonic with period-1 (P1) before $\omega = 7500$ rpm. Accordingly, a single point on each Poincaré map along with distinct peaks at frequencies equal to multiples of the rotational speed indicates P1 motion at $\omega = 6000$ rpm in Fig. 4. Syn-

Author's personal copy

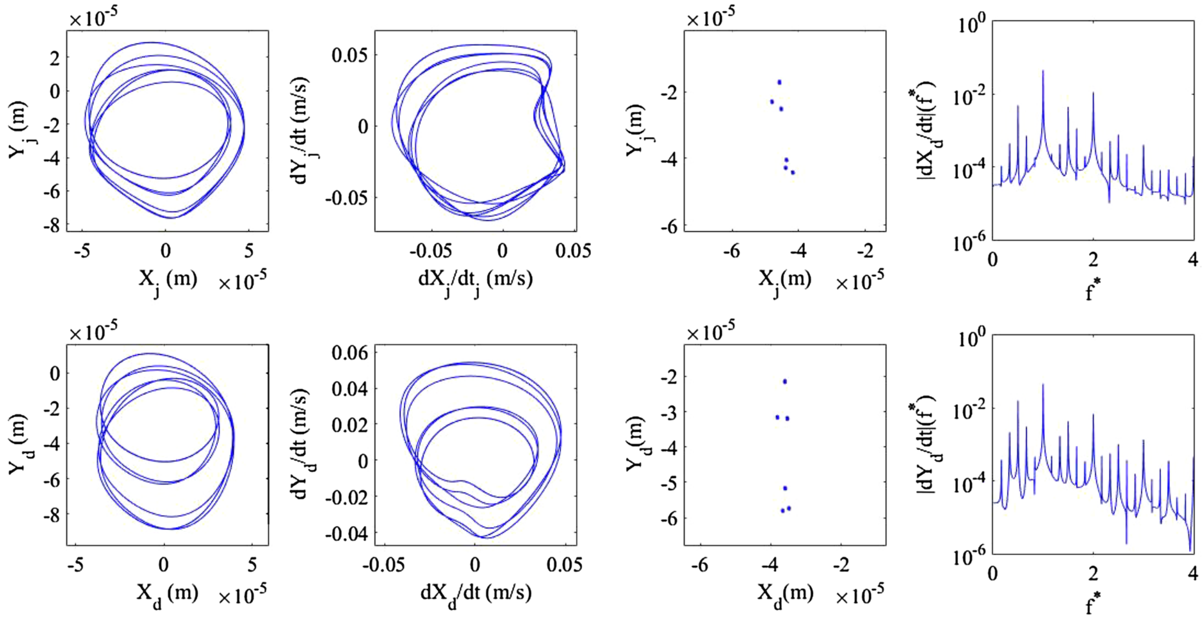

Fig. 8 Phase plane orbits, Poincaré maps and frequency spectra at $\omega = 11{,}400$ rpm

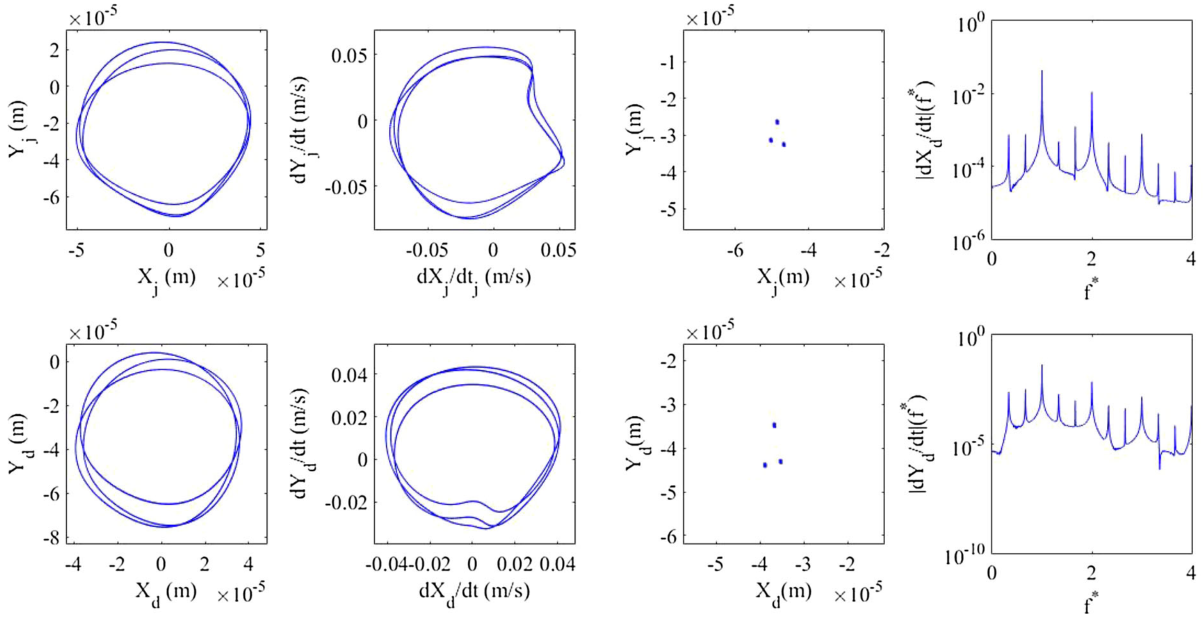

Fig. 9 Phase plane orbits, Poincaré maps and frequency spectra at $\omega = 12{,}100$ rpm

chronous vibrations at $\omega = 6000$ rpm indicate that no contact between the journal and the pads occurs and the oil flow is operating in the hydrodynamic lubrication regime. As the rough surfaces of the journal and the pads are nominally flat, while the oil flow operates in the hydrodynamic lubrication regime, the rotor response evaluated with considering surface roughness leads to the same solution as the one obtained assuming the journal and the pads have smooth surface. This idea is verified by simulating the rotor response based

Author's personal copy

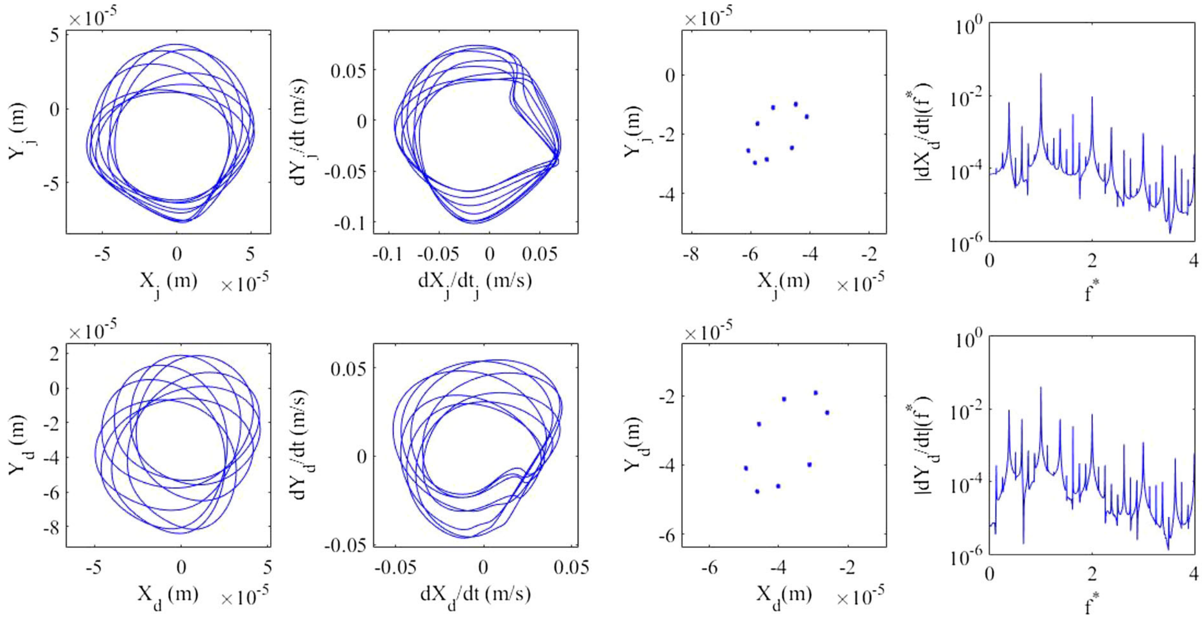

Fig. 10 Phase plane orbits, Poincaré maps and frequency spectra at $\omega = 13{,}200$ rpm

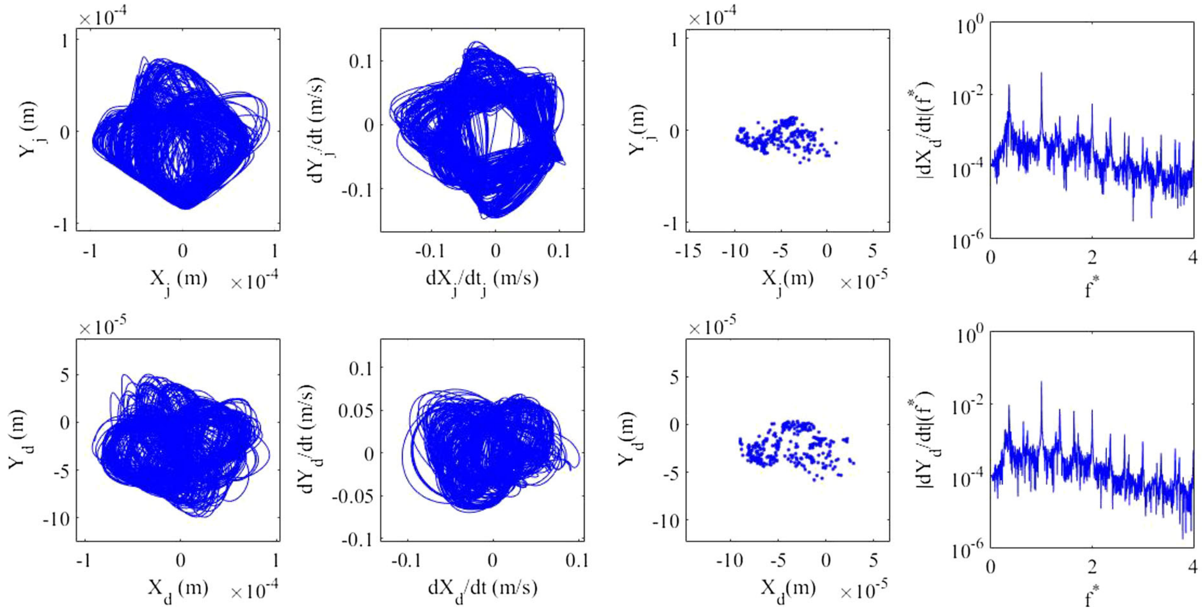

Fig. 11 Phase plane orbits, Poincaré maps and frequency spectra at $\omega = 14{,}300$ rpm

on two different assumptions: the first, assuming the journal and the pads have rough surfaces and the average Reynolds equation [Eq. (12)] governs the oil film lubrication regime, and the second, the surfaces of the journal and the pads are assumed to be smooth and the conventional Reynolds equation governing the oil flow between smooth surfaces is employed. Comparison of system responses with and without considering rough surface assumptions is shown in Fig. 4. It is seen that similar rotor responses are obtained using these two assumptions, which indicates that while the hydrodynamic lubrication regime governs oil flow within the

Author's personal copy

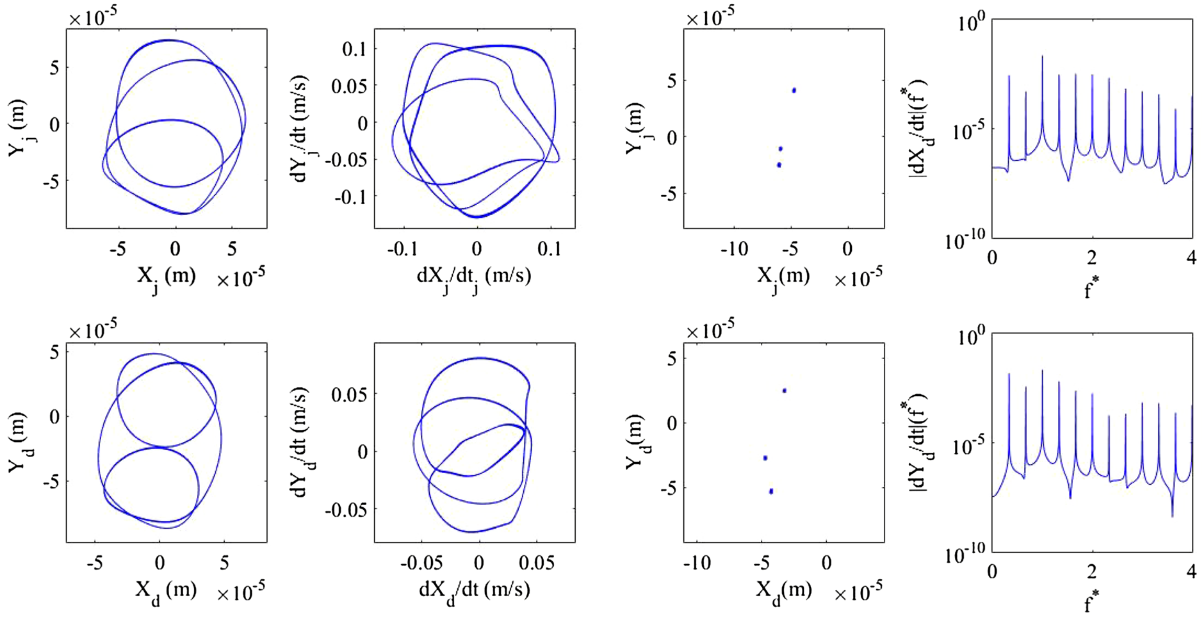

Fig. 12 Phase plane orbits, Poincaré maps and frequency spectra at $\omega = 15{,}900$ rpm

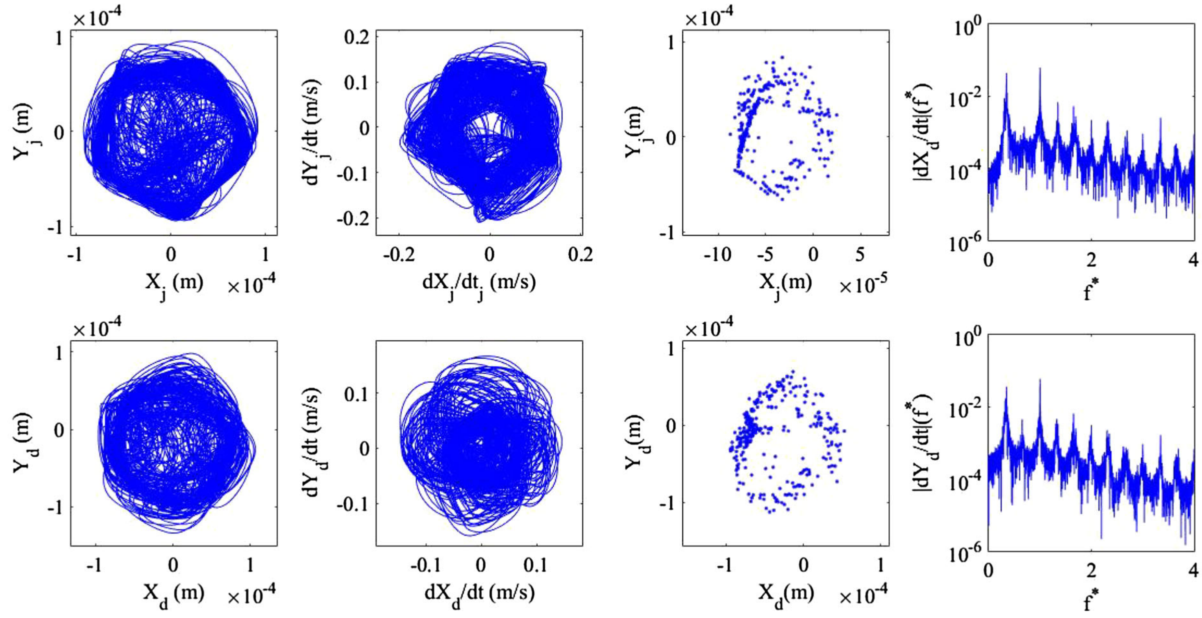

Fig. 13 Phase plane orbits, Poincaré maps and frequency spectra at $\omega = 17{,}700$ rpm

bearing, applying either the smooth surface assumption or the rough surface assumption results in similar rotor response. Bifurcation diagrams in Fig. 2 show that as the rotational speed increases, the dynamic behavior becomes quasiperiodic at ω =[7600–7900] rpm and then it bifurcates to motion with P2 at ω =[8000–11,100] rpm. One can observe quasiperiodic behavior at $\omega = 7800$ rpm and P2 motion at $\omega = 10{,}000$ rpm in Figs. 5 and 6, respectively, through closed curves and two isolated points formed on the associated Poincaré maps. The mean impact force as indicated in Fig. 3 is not significant at ω =[2000–11,100] rpm, except in

Author's personal copy

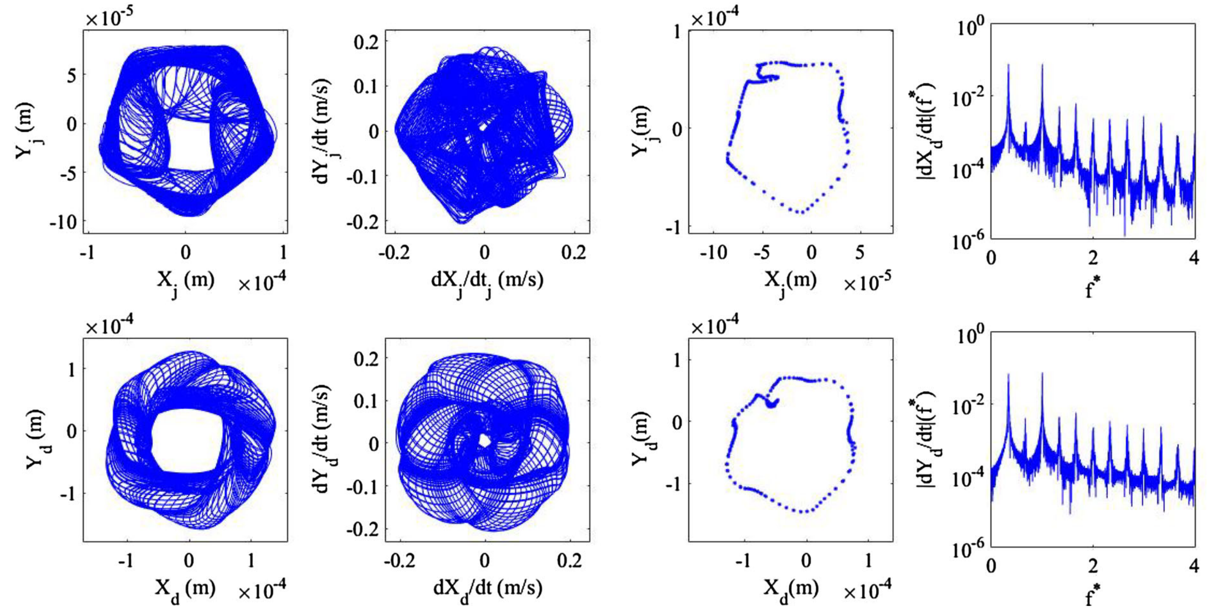

Fig. 14 Phase plane orbits, Poincaré maps and frequency spectra at $\omega = 19{,}500$ rpm

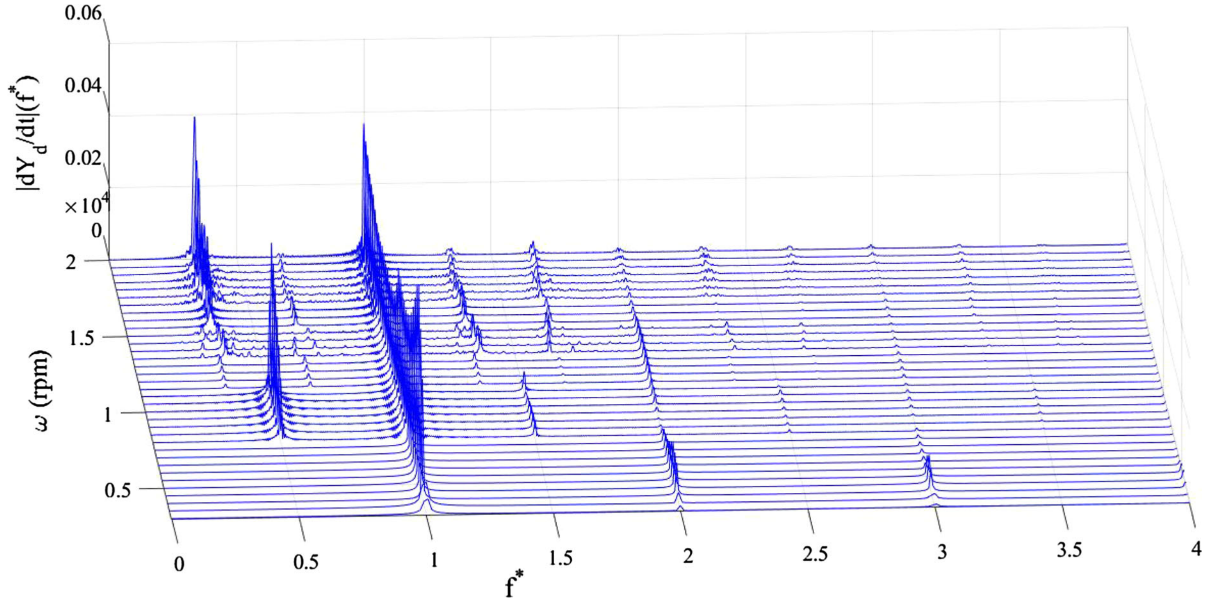

Fig. 15 Waterfall frequency response spectra for disk vertical velocity versus rotational speed

the range $\omega = [2400–3300]$ rpm. While the rotor operates in low-speed range, the journal vibrates in a small orbit close to the two lower pads of the TPJB as indicated by an amount of the non-dimensional vertical displacement of the journal at $\omega = 2000$ rpm. Increase in the rotational speed causes the journal orbit to become larger in size which results in the appearance of the impact force. However, the center of the journal orbit moves upwards to the bearing center by a rise in the rotational speed which prevents the asperity contact to occur between the journal and the pads. Accordingly, it may be concluded that the dynamic behav-

Author's personal copy

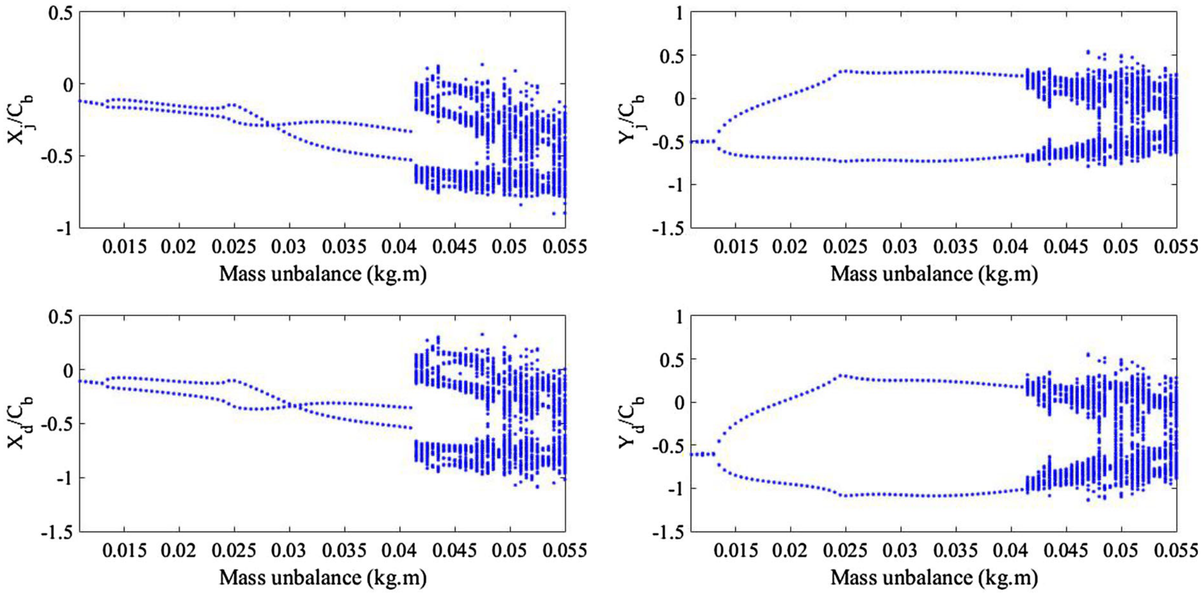

Fig. 16 Bifurcation diagrams of the journal center and the disk center in horizontal and vertical directions at $\omega = 10{,}000$ rpm

Fig. 17 Mean impact force during the steady-state period versus mass unbalance at $\omega = 10{,}000$ rpm

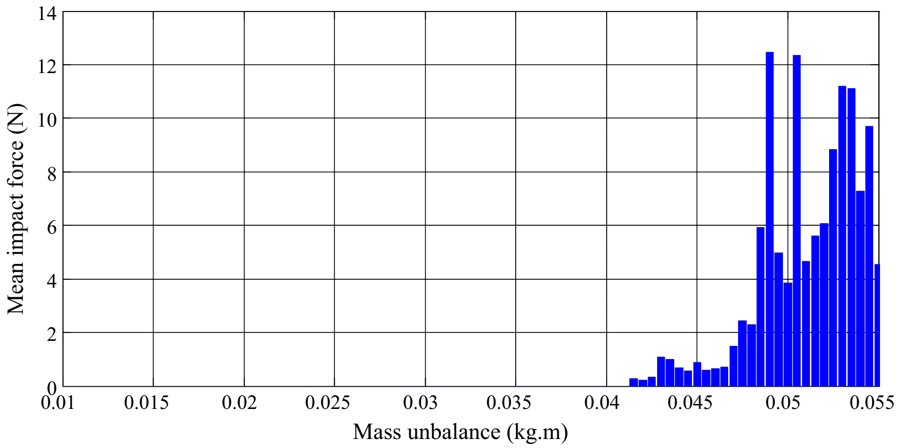

ior of the rotating system at ω = [2400–3300] rpm is more influenced by the orbit size growth than the upward displacement of the journal orbit center, which gives rise to the asperity contact between the journal and the pads. In other words, the rotor–bearing system operating in low speeds, during run-up or shutdown, is prone to be in mixed lubrication condition due to insufficient oil film thickness for properly separating the surfaces of the journal and the pads. The asperity contact between the journal and the pads vanishes beyond $\omega = 3300$ rpm, since the system behavior becomes more affected by the upward movement of the journal orbit center than the continuing growth in the size of the journal orbit. It is found from bifurcation diagrams that the system response becomes chaotic around $\omega = 11{,}200$ rpm. At the same rotational speed in Fig. 3, a sudden rise of the mean impact force appears due to chaotic motion. Low chaotic behavior clarified by two separated region of disordered points on the Poincaré maps at $\omega = 11{,}200$ rpm is shown in Fig. 7. Then, the behavior of the system bifurcates to regular motion with P6 at ω = [11,300–11,500] rpm. In Fig. 8, Poincaré maps with six discrete points and frequency spectra with peaks at multiples of 1/6 of the rotational speed demonstrate P6 behavior at $\omega = 11{,}400$ rpm. As the rotational speed increases fur-

Author's personal copy

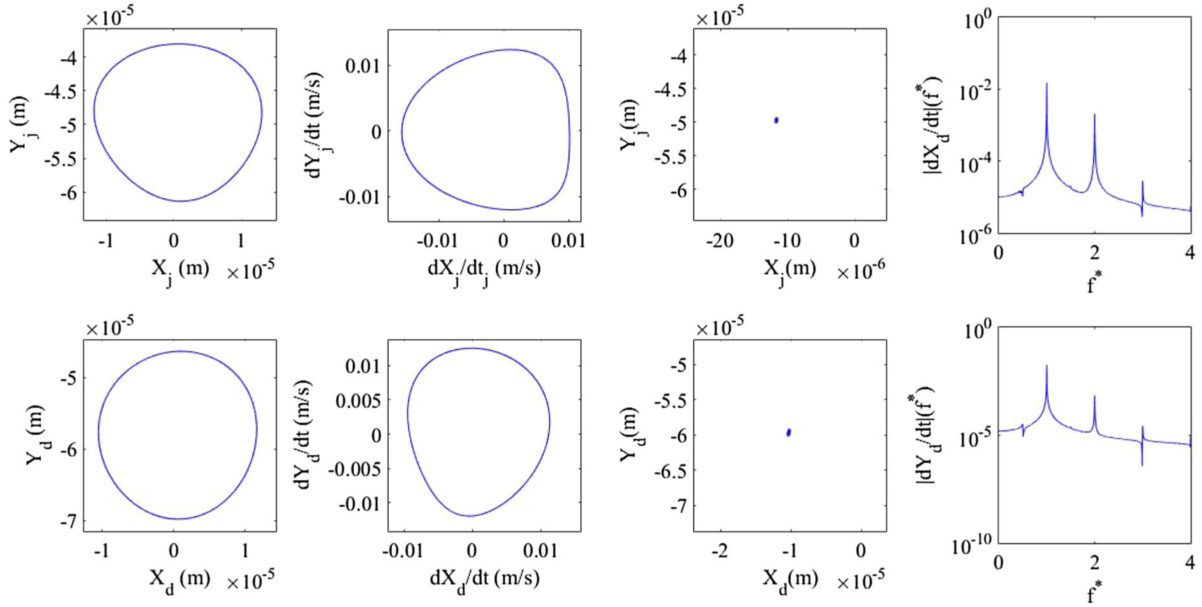

Fig. 18 Phase plane orbits, Poincaré maps and frequency spectra at me = 0.011 kg m

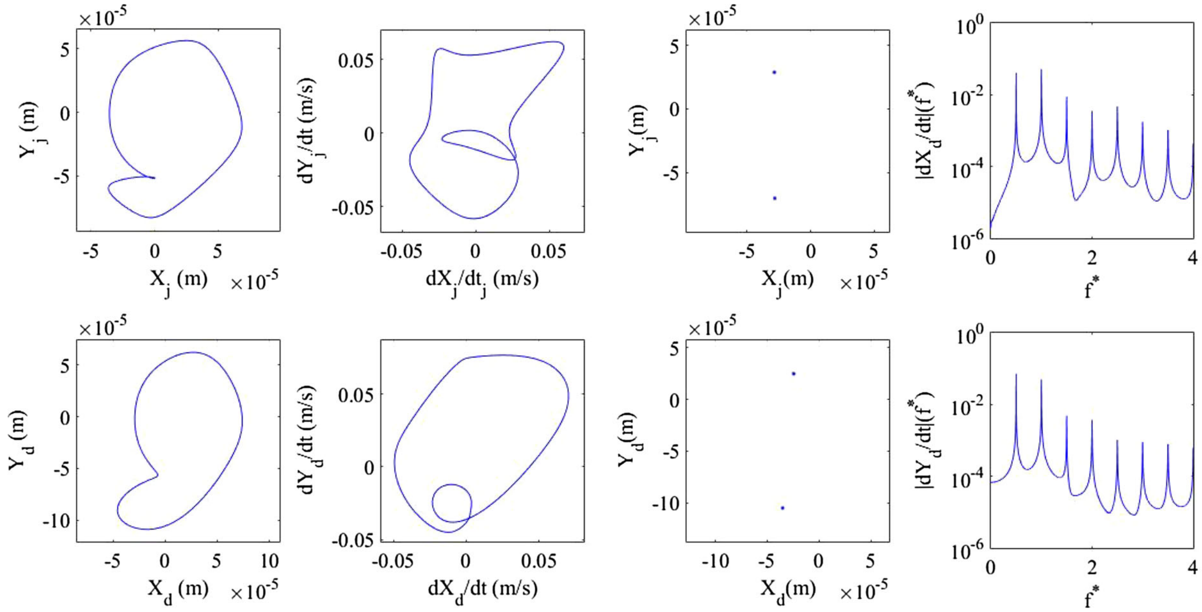

Fig. 19 Phase plane orbits, Poincaré maps and frequency spectra at me = 0.0285 kg m

ther, system response gets into a regular attractor with P3 at $\omega = [11{,}600\text{–}13{,}000]$ rpm. Once the P6 behavior changes to P3 motion, an abrupt increase in the mean impact force is observed in Fig. 3. Regular behavior with P3 at $\omega = 12{,}100$ rpm is displayed in Fig. 9 via three isolated points on the Poincaré maps and peaks at multiples of 1/3 of the rotational speed in the response spectra. Bifurcation from P3 behavior to P8 behavior in a short region of $\omega = [13{,}100\text{–}13{,}200]$ rpm is observed in Fig. 2. Sub-harmonic behavior with P8 is indicated by eight distinct points on the Poincaré maps in Fig. 10. Also, an abrupt increase in the mean impact force is

Author's personal copy

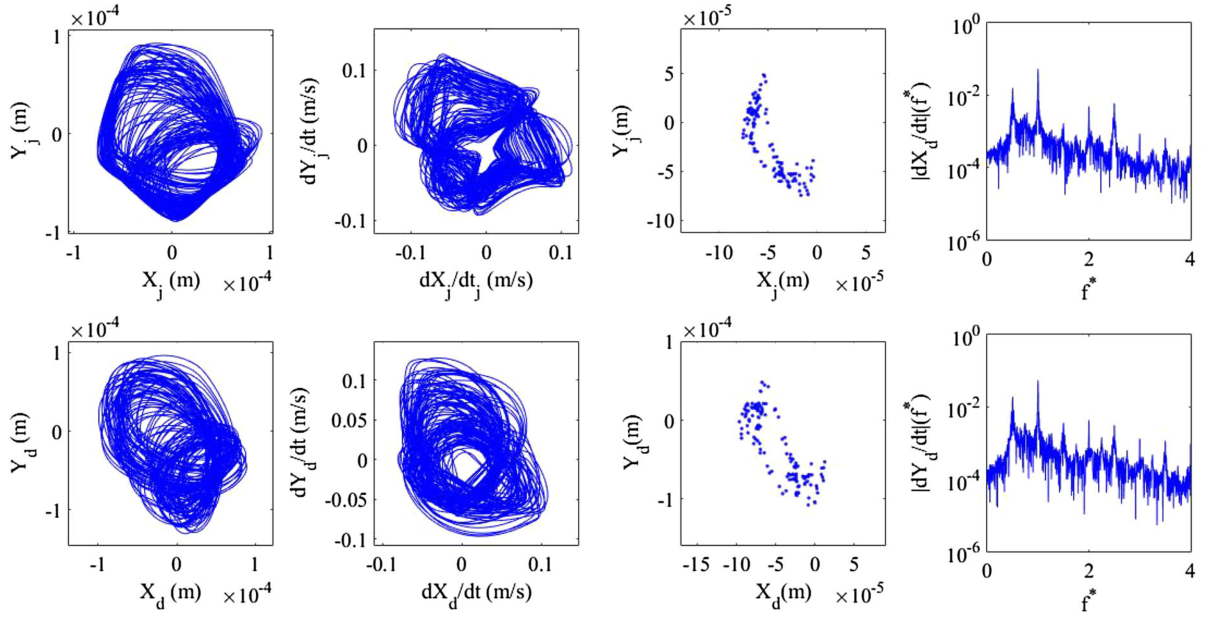

Fig. 20 Phase plane orbits, Poincaré maps and frequency spectra at me = 0.05 kg m

observed in Fig. 3 when the system behavior changes to P8 from P3 at $\omega = 13{,}100$ rpm. An irregular dynamics appears in the system behavior at $\omega = [13{,}300\text{–}15{,}200]$ rpm. The chaotic motion at $\omega = 14{,}300$ rpm is identified by irregularly distributed points forming a fractal geometry on the Poincaré maps shown in Fig. 11. Due to this bifurcation to chaotic motion, the mean impact force decreases sharply at $\omega = 13{,}300$ rpm and continues toward increasing irregularly with respect to the rotational speed. The behavior of the system returns to P3 dynamics at $\omega = [15{,}300\text{–}16{,}700]$ rpm. Once again, bifurcation to P3 motion leads to a sudden increase in the impact force as displayed in Fig. 3. The P3 motion at $\omega = 15{,}900$ rpm is clearly known from the frequency spectra and the Poincaré maps in Fig. 12. The system response bifurcates again to chaotic dynamics at $\omega = [16{,}800\text{–}18{,}700]$ rpm. Bifurcation of the system behavior from P3 motion to chaotic motion results in a sudden drop in the mean impact force at $\omega = 16{,}800$ rpm. The system behavior at $\omega = 17{,}700$ rpm is recognized as chaotic response through irregular points on the Poincaré maps shown in Fig. 13. While the system behaves chaotically, Fig. 3 shows an irregular increasing of mean impact force with respect to the rotational speed. Finally, while the rotational speed goes beyond $\omega = 18{,}800$ rpm, quasiperiodic behavior becomes visible in the rotor response. Closed curves on the Poincaré maps displayed in Fig. 14 indicate the quasiperiodic motion at $\omega = 19{,}500$ rpm. Although the variations of the impact force remain irregular in the region of quasiperiodic state, a small drop of the impact force is observed in Fig. 3 as the dynamics changes from chaotic behavior to quasiperiodic behavior.

Aperiodic motions, including quasiperiodic and chaotic behaviors, are identified within two ranges $\omega = [13{,}300\text{–}15{,}200]$ rpm and $\omega = [16{,}800\text{–}20{,}000]$ rpm in the bifurcation diagrams. Figure 2 shows that the dynamics of the rotor response are qualitatively changed by varying the rotational speed of the rotor. These various dynamic behaviors are accompanying by the changes in the mean impact force, as depicted in Fig. 3. The mean impact force is of a negligible order of magnitude before the response gets instantly into a narrow chaotic band at $\omega = 11{,}200$ rpm. It is interesting to be noticed in Figs. 2 and 3 that the mean impact force levels in sub-harmonic regions with P3 and P8 are significantly higher than the ones in other periodic and irregular regions. Therefore, bifurcations of the unbalance response are significantly affected by increase or decrease in the impact force induced by asperity contacts.

Waterfall frequency response spectra in Fig. 15 give a summary of frequency content of the behavior of the system subject to mass unbalance me = 0.0346 kg m

Author's personal copy

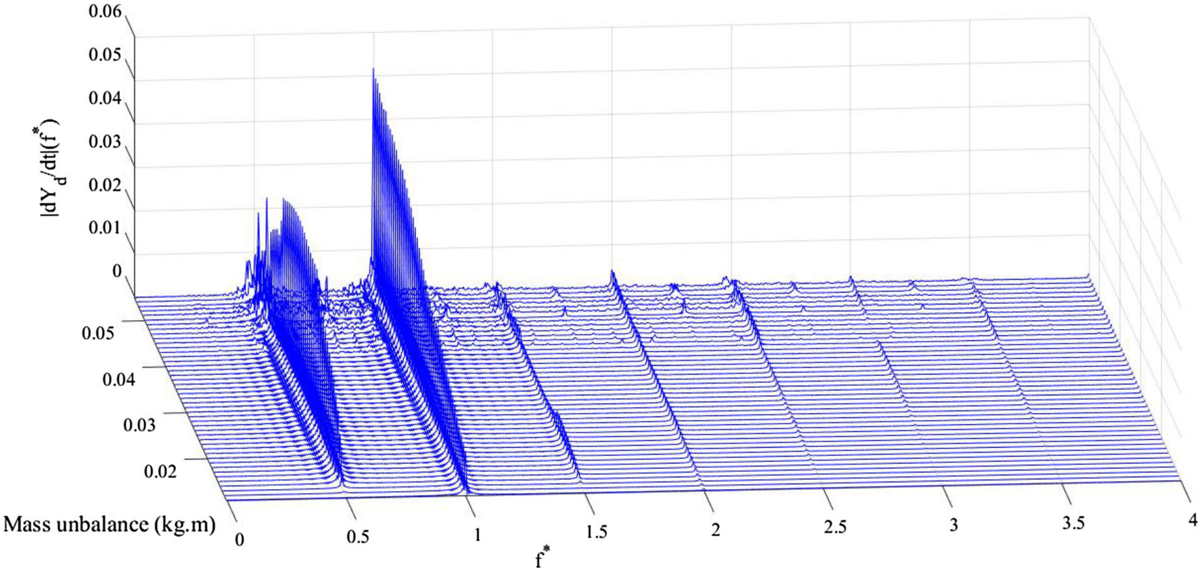

Fig. 21 Waterfall frequency response spectra for disk vertical velocity versus mass unbalance

with variable rotor rotational speed. Sub-harmonies with P2, P3, P6 and P8 are recognized as distinct peaks at multiples of 1/2, 1/3, 1/6 and 1/8 of the rotational speed in Fig. 15, respectively. Spectra of frequencies of quasiperiodic motions are made up of peaks corresponding to irrational fractions of the rotor rotational speed. Chaotic behaviors are identified in waterfall spectra with irregular peaks equal to neither the rational nor irrational fractions of the rotational speed of the shaft.

3.2 Effect of mass unbalance on the rotor response

High unbalanced loads induce strong vibration amplitudes in the rotating machines which result in occurrence of the rub–impact inside the TPJBs. In the underlying rotating system, the unbalanced load is excreted at the disk located in the midplane of the rotor. The qualitative change in the rotor response is illustrated via bifurcation diagrams considering mass unbalance as control parameter shown in Fig. 16. The bifurcations of the behavior of the system are obtained by sampling periodically, with the same period as rotational speed, from the time-series response corresponding to displacements of the journal center and the disk center at $\omega = 10{,}000$ rpm. The mean impact force induced by the asperity contact during the steady-state period with respect to mass unbalance variations at $\omega = 10{,}000$ rpm is depicted in Fig. 17.

While the rotor is excited by the mass unbalance less than me = 0.013 kg m, the rotor response is harmonic with P1. The P1 motion at me = 0.011 kg m is identified by a single point on each Poincaré map in Fig. 18. A period-doubling bifurcation occurs at me = 0.013 kg m, and the dynamic behavior maintains with P2 in the range of me = [0.013–0.041] kg m. Two isolated points on the Poincaré maps indicate P2 motion at me = 0.0285 kg m in Fig. 19. As the mass unbalance exceeds me = 0.041 kg m, the rotor response gets into a chaotic region. According to Fig. 17, the bifurcation from sub-harmonic motion with P2 to chaotic motion results in a sudden rise of the mean impact force. Increasing the mean impact force continues irregularly within the chaotic region as shown in Fig. 17. The irregular points on the Poincaré maps displayed in Fig. 20 indicate the chaotic behavior at me = 0.05 kg m.

The frequency content of the rotor response is displayed through waterfall frequency response spectra in Fig. 21. It is noticed rather than harmonic motions with P1 and P2; no other periodic behaviors exist in the system response within the specified range of mass unbalance. Appearance of the chaotic behavior beyond me = 0.041 kg m is identified with irregular peaks in the waterfall spectra.

Author's personal copy

4 Conclusions

In this study, nonlinear analysis for simulating rub–impact within TPJBs supporting a flexible rotor is carried out. To this end, a rotor–bearing model assuming the oil flow inside the TPJBs in mixed lubrication regime and the elasto-plastic contact between rough surfaces of the pads and the journal are considered. Phase plane orbits, Poincaré maps, waterfall frequency response graphs and bifurcation diagrams are used to analyze the rotor response. The rotational speed and mass unbalance are employed as control parameters to investigate different dynamic behaviors of the rotor–bearing system. Variations of the mean impact force due to asperity contact with respect to the control parameters are evaluated. Various forms of dynamic behaviors such as sub-harmonic, quasiperiodic and chaotic motions are identified by the corresponding bifurcation diagrams and Poincaré maps. Although the onsets of chaotic behaviors in the shown diagrams result in increase in the mean impact force, the impact force levels in sub-harmonic regions with P3 and P8 are of larger amplitudes than the ones in other periodic and irregular regions. It is concluded that abrupt increases and decreases in the impact force lead to qualitative changes in the rotor response. Irregular behaviors such as quasiperiodic and chaotic motions are observed while the system experiences high rotational speed and mass unbalance. The present study provides useful tools for the analysts to diagnose and predict undesirable vibrations happening in experiments due to rub–impact inside industrial journal bearings.

Appendix

The contact between the journal and the kth pad at the point C and their corresponding absolute velocities at this point are displayed in Fig. 22. Since $e \ll R_\mathrm{j}$, the journal absolute velocity can be approximated as:

$$\vec{V}_1 \cong \vec{\omega} \times \overrightarrow{O_\mathrm{J}C}. \tag{A.1}$$

Also, the absolute velocity of the kth pad at the contact point C can be expressed as:

$$\vec{V}_{2,k} = \frac{\mathrm{d}\vec{\delta}_k}{\mathrm{d}t} \times \overrightarrow{PC}, \tag{A.2}$$

where the components of vectors $\overrightarrow{O_\mathrm{J}C}$ and $\overrightarrow{PC}$ in planar Cartesian coordinates are represented as:

$$\overrightarrow{O_\mathrm{J}C} = R_j\left(\cos\theta\vec{\imath} + \sin\theta\vec{J}\right), \tag{A.3}$$

$$\overrightarrow{PC} = |\overrightarrow{PC}|\left(\cos(\gamma - \theta_p)\vec{\imath} + \sin(\gamma - \theta_p)\vec{\imath}\right). \tag{A.4}$$

Applying $e \ll R_\mathrm{j}$, the magnitude of vector $\overrightarrow{PC}$ can be obtained as follows:

$$|\overrightarrow{PC}| = \sqrt{(|\overrightarrow{HP}|)^2 + (|\overrightarrow{HC}|)^2}, \tag{A.5}$$

$$|\overrightarrow{HP}| = |\overrightarrow{O_\mathrm{J}P}| - |\overrightarrow{O_\mathrm{J}H}| \cong R_\mathrm{b} + t_\mathrm{p} - R_\mathrm{j}\cos(\theta - \theta_\mathrm{p}), \tag{A.6}$$

$$|\overrightarrow{HC}| = R_\mathrm{j}\sin(\theta - \theta_\mathrm{p}). \tag{A.7}$$

The sine law is applied to the triangle $O_\mathrm{J}PC$, as shown in Fig. 22, and the direction of vector $\overrightarrow{PC}$ may be determined by:

$$\frac{|\overrightarrow{PC}|}{\sin(\theta - \theta_\mathrm{p})} = \frac{|\overrightarrow{O_\mathrm{J}C}|}{\sin(\gamma)}. \tag{A.8}$$

In order to obtain the direction of friction force applied to the journal, the sign of algebraic difference between the journal absolute velocity and the projected pad absolute velocity on the journal velocity direction has to be determined. The unit vector along the journal absolute velocity at point C is represented as:

$$\vec{e}_1 = -\sin\theta\vec{\imath} + \cos\theta\vec{J}. \tag{A.9}$$

Finally, exerting forces on the journal and the moment on the kth pad resulting from the hydrodynamic and

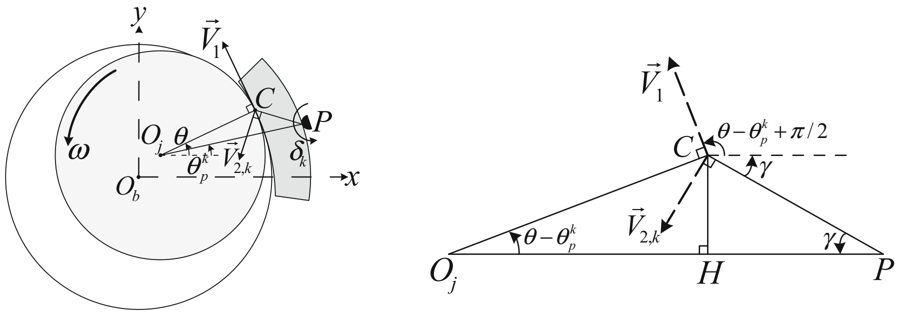

Fig. 22 A display of the contact between the journal and the kth pad

Author's personal copy

asperity contact forces in normal and tangential directions are expressed by:

$$
\begin{aligned}
F_x = &-\sum_{k=1}^{N_{\text{pads}}} \int_{-\frac{L}{2}}^{\frac{L}{2}} \int_{\theta_{\text{s}}}^{\theta_{\text{e}}} ((P_{\text{a},k} + \bar{P}_k)\cos\theta \\
&- \operatorname{sign}((\vec{V}_1 - (\vec{V}_{2,k} \cdot \vec{e}_1)\vec{e}_1) \cdot \vec{e}_1)(\tau_{\text{a},k} + \bar{\tau}_k)\sin\theta) \\
&R_j \mathrm{d}\theta \mathrm{d}z, \qquad \text{(A.10)}
\end{aligned}
$$

$$
\begin{aligned}
F_y = &-\sum_{k=1}^{N_{\text{pads}}} \int_{-\frac{L}{2}}^{\frac{L}{2}} \int_{\theta_{\text{s}}}^{\theta_{\text{e}}} ((P_{\text{a},k} + \bar{P}_k)\sin\theta \\
&+ \operatorname{sign}((\vec{V}_1 - (\vec{V}_{2,k} \cdot \vec{e}_1)\vec{e}_1) \cdot \vec{e}_1)(\tau_{\text{a},k} + \bar{\tau}_k)\cos\theta) \\
&R_j \mathrm{d}\theta \mathrm{d}z, \qquad \text{(A.11)}
\end{aligned}
$$

$$
\begin{aligned}
M_k = &-\int_{-\frac{L}{2}}^{\frac{L}{2}} \int_{\theta_{\text{s}}}^{\theta_{\text{e}}} \Big[-(R_{\text{j}} + t_{\text{p}})(\theta - \theta_{\text{p}}^k)(P_{\text{a},k} + \bar{P}_k) \\
&- \operatorname{sign}((\vec{V}_1 - (\vec{V}_{2,k} \cdot \vec{e}_1)\vec{e}_1) \cdot \vec{e}_1)t_{\text{p}}(\tau_{\text{a},k} + \bar{\tau}_k)\Big] \\
&\cos(\theta - \theta_{\text{p}})R_j \mathrm{d}\theta \mathrm{d}z; \\
&k = 1, \ldots, N_{\text{pads}}. \qquad \text{(A.12)}
\end{aligned}
$$

References

1. Chang-Jian, C.-W., Chen, C.-K.: Chaos and bifurcation of a flexible rub-impact rotor supported by oil film bearings with nonlinear suspension. Mech. Mach. Theory **42**, 312–333 (2007)
2. Chang-Jian, C.-W., Chen, C.-K.: Non-linear dynamic analysis of rub-impact rotor supported by turbulent journal bearings with non-linear suspension. Int. J. Mech. Sci. **50**, 1090–1113 (2008)
3. Chang-Jian, C.-W., Chen, C.-K.: Chaos of rub-impact rotor supported by bearings with nonlinear suspension. Tribol. Int. **42**, 426–439 (2009)
4. Chang-Jian, C.-W., Chen, C.-K.: Nonlinear analysis of a rub-impact rotor supported by turbulent couple stress fluid film journal bearings under quadratic damping. Nonlinear Dyn. **56**, 297–314 (2009)
5. Chang-Jian, C.-W., Chen, C.-K.: Couple stress fluid improve rub-impact rotor–bearing system—nonlinear dynamic analysis. Appl. Math. Model. **34**, 1763–1778 (2010)
6. Wang, J., Zhou, J., Dong, D., Yan, B., Huang, C.: Nonlinear dynamic analysis of a rub-impact rotor supported by oil film bearings. Arch. Appl. Mech. **83**, 413–430 (2013)
7. Xiang, L., Gao, X., Hu, A.: Nonlinear dynamics of an asymmetric rotor–bearing system with coupling faults of crack and rub-impact under oil-film forces. Nonlinear Dyn. **86**, 1057–1067 (2016)
8. Cao, J., Ma, C., Jiang, Z., Liu, S.: Nonlinear dynamic analysis of fractional order rub-impact rotor system. Commun. Nonlinear Sci. Numer. Simul. **16**, 1443–1463 (2011)
9. Abu Arqub, O.: Fitted reproducing kernel Hilbert space method for the solutions of some certain classes of time-fractional partial differential equations subject to initial and Neumann boundary conditions. Comput. Math. Appl. **73**, 1243–1261 (2017)
10. Arqub, O.A., El-Ajou, A., Momani, S.: Constructing and predicting solitary pattern solutions for nonlinear time-fractional dispersive partial differential equations. J. Comput. Phys. **293**, 385–399 (2015)
11. El-Ajou, A., Arqub, O.A., Momani, S.: Approximate analytical solution of the nonlinear fractional KdV–Burgers equation: a new iterative algorithm. J. Comput. Phys. **293**, 81–95 (2015)
12. Spikes, H.A.: Mixed lubrication—an overview. Lubr. Sci. **9**, 221–253 (1997)
13. Patir, N., Cheng, H.S.: An average flow model for determining effects of three-dimensional roughness on partial hydrodynamic lubrication. J. Lubr. Technol. **100**, 12 (1978)
14. Patir, N., Cheng, H.S.: Application of average flow model to lubrication between rough sliding surfaces. J. Lubr. Technol. **101**, 220 (1979)
15. Greenwood, J., Williamson, J.B.P.: Contact of nominally flat surfaces. Proc. R. Soc. A Math. Phys. Eng. Sci. **295**, 300–319 (1966)
16. Johnson, K.L., Greenwood, J.A., Poon, S.Y.: A simple theory of asperity contact in elastohydro-dynamic lubrication. Wear **19**, 91–108 (1972)
17. Yamaguchi, A., Matsuoka, H.: A mixed lubrication model applicable to bearing/seal parts of hydraulic equipment. J. Tribol. **114**, 116 (1992)
18. Ai, X., Cheng, H.S., Hua, D., Moteki, K., Aoyama, S.: A finite element analysis of dynamically loaded journal bearings in mixed lubrication. Tribol. Trans. **41**, 273–281 (1998)
19. Kazama, T., Narita, Y.: Mixed and fluid film lubrication characteristics of worn journal bearings. Adv. Tribol. **2012**, 1–7 (2012)
20. Sander, D.E., Allmaier, H., Priebsch, H.H., Witt, M., Skiadas, A.: Simulation of journal bearing friction in severe mixed lubrication—validation and effect of surface smoothing due to running-in. Tribol. Int. **96**, 173–183 (2016)
21. Leighton, M., Morris, N., Rahmani, R., Rahnejat, H.: Surface specific asperity model for prediction of friction in boundary and mixed regimes of lubrication. Meccanica **52**, 21–33 (2017)
22. Varney, P., Green, I.: Rotordynamic analysis of rotor–stator rub using rough surface contact. J. Vib. Acoust. **138**, 021015 (2016)
23. Asgharifard-Sharabiani, P., Ahmadian, H.: Nonlinear model identification of oil-lubricated tilting pad bearings. Tribol. Int. **92**, 533–543 (2015)
24. Whitehouse, D.J., Archard, J.F.: The properties of random surfaces of significance in their contact. Proc. R. Soc. A Math. Phys. Eng. Sci. **316**, 97–121 (1970)
25. Johnson, K.L.: Contact Mechanics. Cambridge University Press, Cambridge (1985)
26. Greenwood, J.A., Tripp, J.H.: The contact of two nominally flat rough surfaces. Proc. Inst. Mech. Eng. **185**, 625–633 (1970)